



Cite this: *New J. Chem.*, 2021, 45, 6247

Bi₂O₂CO₃/TiO₂ hybrid with 0D/1D nanostructure: design, synthesis and photocatalytic performance†

Yanwei Wang,^{‡a} Jiayi Li,^{‡a} Bowei Wang,^{id *abc} Mingming Sun,^a Xilong Yan,^{id abc} Ligong Chen,^{id abc} Guoyi Bai^{id d} and Yang Li^{id *abc}

Photocatalytic technology is a potential technology to meet energy and environmental requirements. Herein, the solvothermal method was used for the first time to synthesize a Bi₂O₂CO₃/TiO₂ hybrid with 0D/1D nanostructure, and the obtained materials were characterized systematically. In the architecture of the composite, Bi₂O₂CO₃ quantum dots (QDs) (1.40–1.50 nm) uniformly grew on the surface of TiO₂ nanobelts (NBs). The degradation efficiency of Rhodamine B under visible light irradiation was applied to evaluate the photocatalytic performance of the obtained materials. Of them, TB-3 exhibited the best photocatalytic performance, and more than 95.43% RhB was degraded under visible light. The reaction rate constant is $18.51 \times 10^{-3} \text{ min}^{-1}$, which is nine times larger than that of TiO₂ NBs. Moreover, it exhibited remarkable stability and recyclability in a recycling experiment. According to the photoelectric characterization, the excellent performance may be attributed to the construction of a heterojunction and hybrid structure with 0D Bi₂O₂CO₃ QDs and 1D TiO₂ NBs, which endows the catalyst with faster migration of photo-generated carriers and less recombination of electron/hole pairs. Our work provides a promising method to build novel visible light-driven photocatalysts with a 0D/1D hybrid structure.

Received 18th January 2021,
 Accepted 4th March 2021

DOI: 10.1039/d1nj00281c

rsc.li/njc

1. Introduction

Water pollution, especially organic contaminants, is a great hazard to public health and ecosystems, and is a problem that urgently needs to be solved.^{1–3} Among various methods to treat the organic pollutants in wastewater, photocatalytic technology has been carried out extensively as it is sustainable and eco-friendly.^{1–3} So far, many semiconductor photo-catalysts have been developed, such as TiO₂, Bi₂O₂CO₃, C₃N₄, MoS₂, etc.^{4–9}

TiO₂ has attracted significant attention due to chemical stability, appropriate band structure and low cost.¹⁰ However, owing to its large band gap and high recombination rate of photo-generated carriers, its application is seriously restricted.¹¹ In order to enhance the photocatalytic performance of TiO₂, a number of modification methods have been proposed.^{12–14}

Considering the great impact of morphology for nanostructured materials, the adjustment of the morphology for TiO₂ has attracted widespread attention. Among them, 1D TiO₂ nanobelts (NBs) have achieved remarkable results due to the advantages^{15–19} of larger surface area,¹⁵ higher migration of carriers in the axial direction¹⁶ and excellent recyclability.¹⁷ Moreover, the nanobelts can be used as a substrate to grow other components and construct heterostructures.^{14,18,19} In our previous work,²⁰ a graphene modified TiO₂ NB hybrid was synthesized and displayed excellent performance in the degradation of MO and MB under UV irradiation. The synergistic effect between the two components promotes the effective separation of charges. Therefore, the construction of a hybrid nanostructure is an effective way to construct a heterostructure and improve the photocatalytic activity, which has been proven as an efficient method to prevent the recombination of photogenerated electron/hole pairs in semiconductors.^{14,20}

Furthermore, Bi₂O₂CO₃ as an indirect bandgap semiconductor has received extensive attention in the field of photocatalysis.^{6,21–23} In 2010, Cheng *et al.*⁶ reported the synthesis of 3 μm Bi₂O₂CO₃ microflowers *via* the solution method for degradation of MO under UV light. Then, Y. Lian *et al.*²⁴ reported the synthesis of Bi₂O₂CO₃/TiO₂ composites, which can efficiently catalyze the degradation of Rhodamine B (RhB) under UV illumination, and it confirmed that charges can be transferred between Bi₂O₂CO₃ and TiO₂. However, the photocatalytic performance of the material was unsatisfactory

^a School of Chemical Engineering and Technology, Tianjin University, Tianjin 300350, China. E-mail: bwwang@tju.edu.cn, lityang777@tju.edu.cn

^b Collaborative Innovation Center of Chemical Science and Engineering (Tianjin), Tianjin 300072, China

^c Tianjin Engineering Research Center of Functional Fine Chemicals, Tianjin, China

^d College of Chemistry and Environmental Science, Hebei University, Baoding 071002, P. R. China

† Electronic supplementary information (ESI) available. See DOI: 10.1039/d1nj00281c

‡ These authors contributed equally to this work.

under visible light. To date, although there have been many studies on $\text{Bi}_2\text{O}_2\text{CO}_3$ catalysts, all of them were concentrated on the micron-size $\text{Bi}_2\text{O}_2\text{CO}_3$ whose applications were still limited by poor utilization of visible light and high recombination rate of photo-generated carriers. Quantum dots (QDs) with shorter charge-migration distance were frequently used to construct the hybrid nanostructure. The material with this structure has achieved excellent photocatalytic performance under visible light because of the characteristics of large interface area and ultra-fast carrier transportation.^{25–27}

Based on the above, we tried to take advantage of the easy assembly of TiO_2 NBs and ultra-fast charge transport of $\text{Bi}_2\text{O}_2\text{CO}_3$ QDs to develop a novel $\text{Bi}_2\text{O}_2\text{CO}_3/\text{TiO}_2$ hybrid with a 0D/1D nanostructure (TB-3). The photocatalytic performance of the material was investigated by the degradation of RhB under visible light irradiation. As predicted, the material exhibited excellent photocatalytic performance. The obtained materials were characterized systematically. The construction of 0D $\text{Bi}_2\text{O}_2\text{CO}_3$ QDs and 1D TiO_2 NBs can reduce the band gap, as well as promote ultra-fast charge transfer and efficient separation, which greatly improved the visible-light-driven degradation efficiency.

2. Experimental section

2.1. Chemicals

Ethanol, titanium(IV) butoxide, acetic acid, lithium acetate dehydrate, *N,N*-dimethylformamide, bismuth nitrate pentahydrate ($\text{Bi}(\text{NO}_3)_3 \cdot 5\text{H}_2\text{O}$), ethylene glycol (EG), sodium sulphate (Na_2SO_4), *t*-butyl alcohol (*t*-BuOH), ethylenediaminetetraacetic acid disodium (EDTA-2Na) and benzoquinone (BQ) were purchased and used as analytical grade without further purification.

2.2. Catalyst preparation

TB catalysts were prepared *via* a solvothermal method. Typically, a certain amount of $\text{Bi}(\text{NO}_3)_3 \cdot 5\text{H}_2\text{O}$ and 96.0 mg TiO_2 NBs prepared by a typical preparation process²⁸ were dispersed in 40.0 mL EG to form a uniform solution under vigorous stirring. The above solution was transferred to a Teflon-sealed autoclave and kept at 180 °C for 6 hours. After being cooled to room temperature, the product was collected through centrifugation and washed several times with distilled water before freeze drying. According to the masses of $\text{Bi}(\text{NO}_3)_3 \cdot 5\text{H}_2\text{O}$ (12.0, 24.0, 36.0, 48.0, 60.0 mg), the materials were named as TB-1, TB-2, TB-3, TB-4, and TB-5, respectively.

2.3. Characterization of materials

X-ray diffraction (XRD) patterns were obtained with an X-ray diffractometer (PANalytical X'Pert PRO), employing Cu-K α radiation, the scanning range is 20–80°, and the scanning speed is 4° min⁻¹. Microstructures and surface morphologies were observed on a Hitachi S-4800 scanning electron microscope (SEM) and JEOL JEM-F200 transmission electron microscope (TEM). BET surface area data were acquired by a NOVE 2000e (Quantachrome). The chemical valence states of materials were detected

by X-ray photoelectron spectroscopy (K-Alpha+ spectrometer, ThermoFisher Scientific) with Al K α radiation. The intermediates were detected with an Ultra Performance Liquid Chromatography-Triple Quadrupole Tandem Mass Spectrometer (UPLC-MS/MS, Xveo TQ-XS) with an electrospray ionization source.

2.4. Photoelectric characterization

The photocatalytic activities of the obtained materials were investigated by degradation of RhB under visible irradiation ($\lambda > 420$ nm) at room temperature. In a typically experiment, 12.5 mg material was dispersed in 20.0 mg L⁻¹ RhB (25.0 mL) aqueous solution. Before irradiation, the suspensions were kept in the dark for 45 min to establish adsorption/desorption equilibrium. A 450 W Xe arc lamp (CEL-LAB500E4) with a filter ($\lambda = 420$ nm) was applied as a visible light source. 2.5 mL of the suspension was collected every 0.5 h, and the concentration of RhB was tested with a UV-visible spectrophotometer (L8 Shanghai INESA Scientific Instrument Co., Ltd, China) to evaluate the photocatalytic activity of the material for the degradation of RhB.

In the active species-trapping experiments, 5.0 mM EDTA-2Na, 5.0 mM *t*-BuOH and 5.0 mM BQ were employed as the scavenger of holes (h^+), hydroxyl radicals ($\cdot\text{OH}$) and electrons ($\cdot\text{O}_2^-$), respectively. Under the same conditions of the light reaction experiment, the active species-trapping experiments were carried out. UV-vis-NIR diffuse reflectance spectra (DRS) were recorded on a PE Lambda 750 spectrophotometer with an integrating sphere attachment in the range of 200–800 nm and with BaSO_4 used as the reflectance standard. Photoluminescence (PL) spectra of different materials were obtained by a Fluorolog3 spectrofluorometer (excitation wavelength is 260.0 nm). The electrochemical impedance spectroscopy (EIS) was tested under the amplitude of alternating current voltage (AC) of 5.0 mV. Ruthenium–titanium mesh was used as the auxiliary electrode. The saturated calomel electrode (SCE) was used as the reference electrode, and 0.5 M Na_2SO_4 aqueous solution was used as the electrolyte solution. The electrochemical measurement was performed on an electrochemical workstation (CHI660D).

3. Results and discussion

3.1. Physical properties of the materials

3.1.1. XRD analysis. The crystal structure information was examined by XRD measurement. As shown in Fig. 1, the diffraction peaks of TiO_2 are consistent with those of anatase phase TiO_2 (PDF#86-1156) and rutile phase TiO_2 (PDF#21-1276), indicating the dual crystal phase structure of anatase and rutile.^{29–31} The TB-3 inherits the diffraction peaks of TiO_2 , confirming that the crystal phase of TiO_2 was not destroyed during the prepared processing. In addition, the diffraction peaks at 23.90°, 30.30°, 32.73°, and 52.24° in TB-3 are contributed by the (121), (161), (002) and (2120) crystal planes of $\text{Bi}_2\text{O}_2\text{CO}_3$, indicating the successful preparation of $\text{Bi}_2\text{O}_2\text{CO}_3$. At the same time, the average grain sizes of TiO_2 and TB-3 were calculated by the Scherrer formula. Among them, the average grain sizes of the TiO_2 and TB-3 are 19.67 nm and 21.07 nm, respectively, which indicates that the introduction of

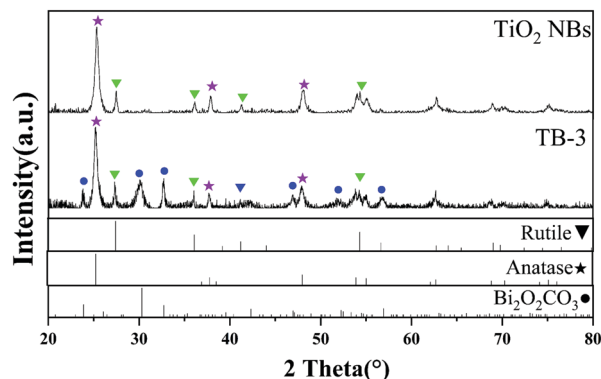


Fig. 1 XRD patterns of TiO_2 and TB-3.

$\text{Bi}_2\text{O}_2\text{CO}_3$ QDs slightly increases the average grain size of the catalyst.

3.1.2. SEM, TEM, STEM, SAE and EDX analysis. To explore the morphology and microstructure of materials, SEM and HRTEM were employed. As revealed in Fig. 2a, TiO_2 presents as uniform strip-like structure. And as the HRTEM image shows in Fig. 2c, TiO_2 presents as smooth nanobelts³² with the width of 6.9 nm and the length of 200.0 nm. Its lattice spacings of 0.32 nm and 0.35 nm are well assigned to the (110) crystal plane of rutile and the (101) crystal plane of anatase, respectively. The clear dual-crystalline structure of TiO_2 NBs is consistent with the XRD result. Meanwhile, according to Fig. 2b and the lattice spacings in Fig. 2d, TB-3 obviously inherits the strip-like morphology and dual-crystalline structure, which proves that the

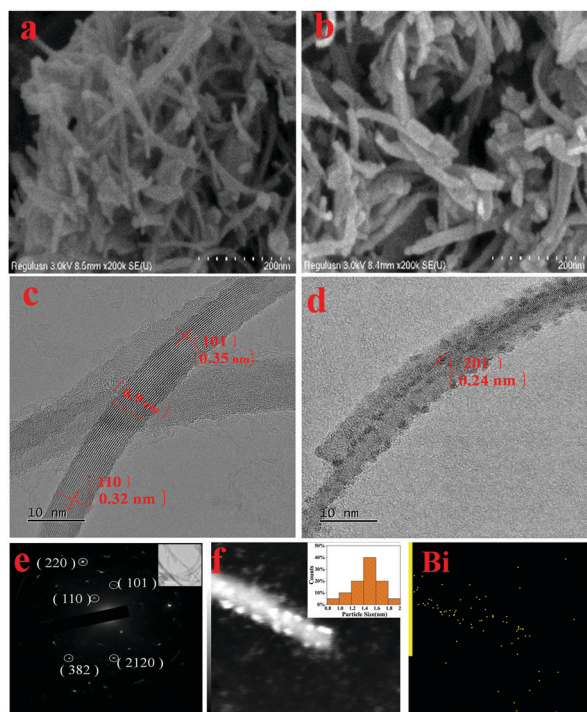


Fig. 2 SEM images of (a) TiO_2 and (b) TB-3. HRTEM images of (c) TiO_2 and (d) TB-3. (e) TEM image of TB-3 and the corresponding SAED pattern. (f) STEM image with size distribution and the corresponding mapping of TB-3.

subsequent processing cannot destroy the TiO_2 NB structure. However, unlike the smooth surface of TiO_2 NBs, TB-3 is presented as narrow belts decorated with many uniform 0D nanoparticles with diameter less than 10 nm on the surface. And the lattice spacing of 0.24 nm is attributed to the (201) crystal plane of $\text{Bi}_2\text{O}_2\text{CO}_3$, which proves that the nanoparticles dispersed on the surface of the nanobelts were $\text{Bi}_2\text{O}_2\text{CO}_3$. Furthermore, typical electron diffraction patterns of TiO_2 and $\text{Bi}_2\text{O}_2\text{CO}_3$ are discovered in TB-3 shown in Fig. 2e. Within the elected area (inserted image in Fig. 2e), the diffraction spots belonging to the (110) and (220) planes of anatase phase, the (101) plane of rutile phase and the (382) and (2120) planes of $\text{Bi}_2\text{O}_2\text{CO}_3$ are found. Moreover, the elemental mapping of Bi in TB-3 (Fig. 2f) coincides with the nanoparticles with a typical diameter of 1.40–1.50 nm, further indicating that the $\text{Bi}_2\text{O}_2\text{CO}_3/\text{TiO}_2$ hybrid with a 0D/1D nanostructure was successfully constructed as expected.

3.1.3. BET analysis. The porous structure and specific surface area of TiO_2 NBs and TB-3 were analysed by N_2 adsorption–desorption measurement, and the results are shown in Fig. 3. For TiO_2 NBs, the BET specific area is $83.36 \text{ m}^2 \text{ g}^{-1}$, the pore size is 12.65 nm, and the isotherm of TiO_2 NBs belongs to the type V pattern. By contrast, TB-3 has a larger surface area ($121.49 \text{ m}^2 \text{ g}^{-1}$) and the pore size is 12.24 nm. Meanwhile, for TB-3, the isotherm is close to the type V pattern with H3-type hysteresis loops, which is almost the same as TiO_2 NBs. There is a negligible peak in the pore-size distribution curves which can be derived from the pores between the aggregated nanobelts,³³ and no mesopores appear on the nanobelts of TB-3. QDs with a larger surface area show excellent photocatalytic activity, and thus the introduction of $\text{Bi}_2\text{O}_2\text{CO}_3$ QDs may be beneficial to improve the photoactivity.³⁴

3.1.4. XPS analysis. The surface composition and chemical states of TB-3 were characterized by XPS. In the full-scan XPS (Fig. 4a), it is determined that TB-3 is composed of Bi, C, O and Ti. The XPS spectrum of Ti 2p in Fig. 4b shows two broad peaks with binding energy of 458.50 eV and 464.30 eV, which are assigned to Ti 2p_{3/2} and Ti 2p_{1/2} of Ti^{4+} respectively. As shown in Fig. 4c, the XPS spectrum of Bi 4f exhibits two XPS peaks located at 158.74 eV and 164.07 eV, which are contributed by $\text{Bi}^{3+} 4f_{7/2}$ and $\text{Bi}^{3+} 4f_{5/2}$ respectively. The O 1s spectrum (in Fig. 4d) can be fitted with four typical peaks, which are ascribed to adsorbed H_2O (532.40 eV),³⁵ Bi–O bands (529.50 eV),³⁶ Ti–O bands (529.90 eV)³⁶ and carbonate species (531.30 eV),³⁵ and the existence of Bi–O bands and carbonate species proves the existence of $\text{Bi}_2\text{O}_2\text{CO}_3$.

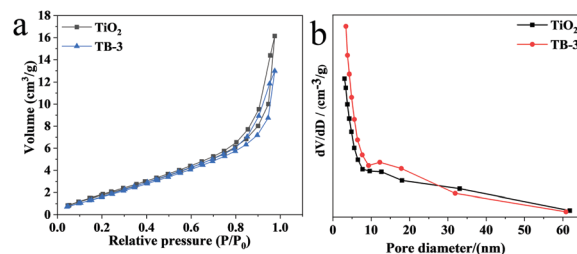


Fig. 3 (a) N_2 adsorption–desorption isotherms. (b) The pore-size distribution curves.

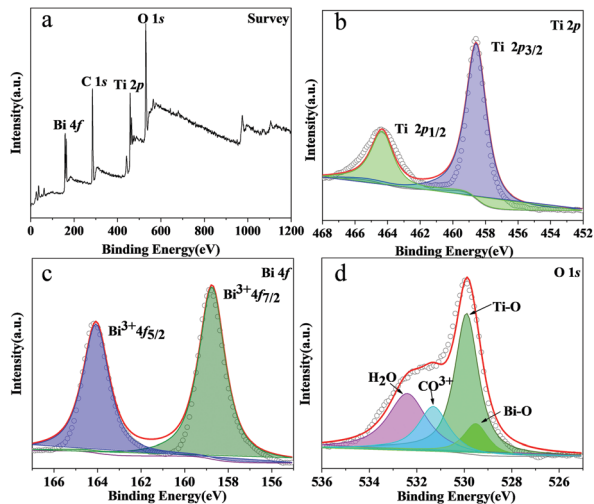


Fig. 4 (a) The full-scan XPS spectra for TB-3. XPS spectra of (b) Ti 2p, (c) O 1s and (d) Bi 4f for TB-3.

3.1.5. FT-IR spectra. Fig. 5 shows FT-IR spectra of TiO₂ and TB-3. The peaks at 3422 and 1629 cm⁻¹ can be ascribed to the stretching and deformation vibration of O–H. Notably, as shown in the detailed pattern, compared with typical TiO₂ bands, the new stretches at 1454 and 1097 cm⁻¹ in TB-3 are contributed to the asymmetric vibration and the symmetric stretching mode of the carbonate, and the peak at 1125 cm⁻¹ is the characteristic peak of the synergistic vibrational effect of C–Bi and Bi–O–Bi bonds. These stretches prove the formation of Bi₂O₂CO₃.

3.2. Photoelectric performance of the samples

The UV-vis-DRS of TiO₂ NBs and TB-3 was recorded. As displayed in Fig. 6a, due to the dual-crystalline structure of TiO₂ NBs, there is a faint absorption in the TiO₂ NBs around 400 nm.^{29–31} By contrast, TB-3 shows an obvious absorption in the range from 200–to 800 nm, which may be due to the introduction of Bi₂O₂CO₃ QDs.³⁷ According to the transformed Kubelka–Munk function, the band gap of TiO₂ NBs is 3.01 eV (inserted image in Fig. 6a). Meanwhile, the band gap of TB-3 is 2.91 eV, much smaller than that of TiO₂ NBs. This may be ascribed to the

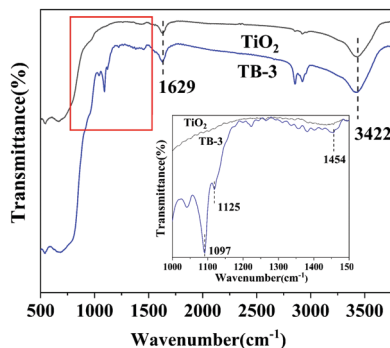


Fig. 5 FT-IR spectra of TiO₂ and TB-3, and the corresponding enlarged details of the FT-IR spectra.

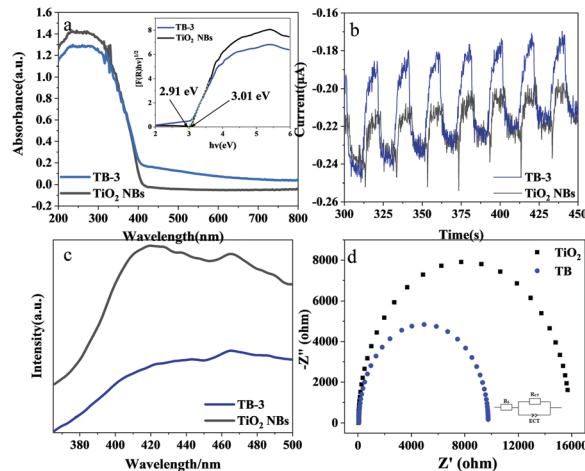


Fig. 6 (a) UV-vis-DRS and plot of Kubelka–Munk function versus energy of TiO₂ NBs and TB-3. (b) Transient photocurrent responses of TiO₂ NBs and TB-3. (c) PL spectra of TiO₂ NBs and TB-3. (d) EIS of TiO₂ NBs and TB-3.

interfacial interaction between the two components.³⁷ Then, the transient photocurrent responses of TiO₂ NBs and TB-3 are determined to evaluate the separation of photogenerated electron/hole pairs (Fig. 6b). Compared with TiO₂ NBs, stronger optical flow intensity of TB-3 may be attributed to the introduction of Bi₂O₂CO₃ QDs with an ultra-fast carrier transport ability.³⁸ Furthermore, the PL spectra were measured to investigate the recombination of the photo-generated carriers of the material. As shown in Fig. 6c, the lower intensity of the curve indicates that the recombination of photo-generated holes and electrons is inhibited in TB-3. The EIS was also performed to investigate the photoelectron transfer. Compared with 1D TiO₂ NBs, the smaller semicircle arc of the TB-3 sample is observed in Fig. 6d, implying that TB-3 successfully decreases the charge-transfer resistance. This may be caused by the reason that Bi₂O₂CO₃ QDs acting as excellent electron acceptors with shorter charge-migration distance are beneficial for charge transfer and separation in TB-3.³⁹

RhB was used as a typical organic pollutant to evaluate the photocatalytic performance of the synthesized materials under visible light irradiation. As shown in Fig. 7a, the concentration of RhB remains almost changeless after 2.5 hour under visible light irradiation without any catalyst (Blank), which proves the stability of RhB. Under the same conditions, TB-3 exhibits excellent degradation efficiencies of 95.34% compared with pure TiO₂ NBs (28.77%). Considering that the photocatalytic degradation process of RhB followed the quasi-first order reaction kinetics, the reaction rate constant (*K*) was calculated and displayed in Fig. 7b. Thereinto, the largest *K* belongs to TB-3 (*K* = 18.51 × 10⁻³ min⁻¹), which is nine times larger than that of TiO₂ NBs. Obviously, the introduction of Bi₂O₂CO₃ QDs significantly improves the photocatalytic activity of TB-3 under visible light. According to the characterization results, we speculate that the combination of 0D Bi₂O₂CO₃ QDs and 1D TiO₂ NBs plays an important role in facilitating the photodegradation of RhB, and TB-3 possesses a narrower band gap.⁴⁰ Furthermore, charges can be transferred from TiO₂ NBs to

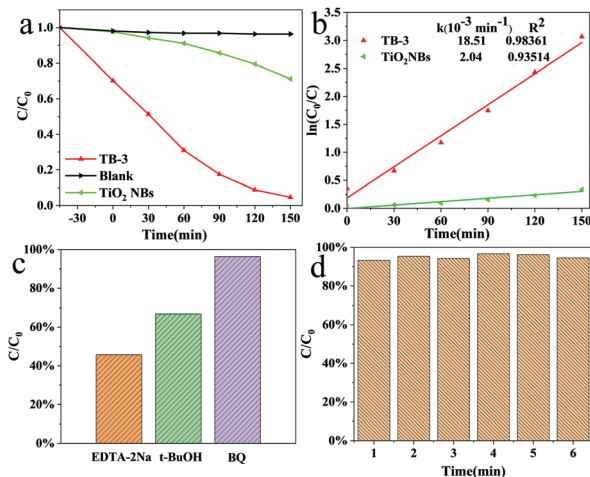


Fig. 7 (a) Photocatalytic activities of blank, TiO₂ NBs and TB-3 under visible light irradiation. (b) Plot of $\ln(C_0/C)$ versus time. (c) Results of active species-trapping experiments. (d) Recycling experiment of TB-3.

Bi₂O₂CO₃ QDs, which facilitates the separation of carriers.^{27,37} In addition, as the Bi₂O₂CO₃ QDs have smaller size and shorter charge-migration distance, carriers are more likely to conduct ultra-fast transfer. Therefore, the recombination of photo-generated holes and electrons is reduced, which is also consistent with the PL spectrum.²¹ Moreover, the introduction of Bi₂O₂CO₃ QDs also increases the surface area of TB materials, which is beneficial for light adsorption and mass transfer. Compared with other TB samples, TB-3 exhibits the best photocatalytic activity (image in Fig. S1 and S2, ESI[†]), which may be due to the higher crystallinity and better carrier-transport capability of Bi₂O₂CO₃ QDs.⁴¹

To explore the main active species in the degradation process of RhB, different scavengers were employed. As shown in Fig. 7c, when BQ was added to the reaction system, there is no obvious drop in the photocatalytic degradation of RhB. However, with the addition of EDTA-2Na and *t*-BuOH, the degradation efficiency decreases visibly, which implies that h^+ and $\cdot\text{OH}$ are the main active species to degrade RhB in the reaction system.

In order to study the stability and reusability of TB-3, recycling experiments were carried out. As displayed in Fig. 7d, the photo-degradation activity of TB-3 does not drop obviously in six cycles, illustrating the excellent recyclability. The XRD pattern and STEM image of recycled TB-3 (Fig. S3, ESI[†]) display similar to those of a fresh sample. These results fully demonstrated that TB-3 is extremely robust.

3.3. Mechanism research

3.3.1. Pollutant degradation mechanism. Temporal UV-visible adsorption spectral change was used to explore the photo-degradation process of RhB, and the result is shown in Fig. 8. After 150 minutes of visible light irradiation, the absorption peak of the solution gradually blue-shifts from 554 to 498 nm, which is caused by the *N*-deethylation of RhB during the photocatalytic degradation.⁴² According to the UPLC-MS/MS spectrum (Fig. S4, ESI[†]), a schematic diagram of the reaction

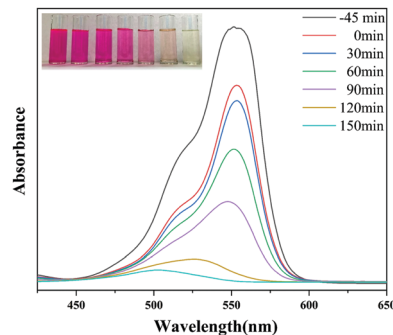


Fig. 8 The temporal UV-visible adsorption spectral change of the RhB at different times.

process is summarized in Fig. S5 (ESI[†]). The degradation process of RhB is the gradual removal of ethyl groups and the continued mineralization. As shown in the 150 minute UPLC-MS/MS spectrum, there are no by-product peaks except for a negligible peak of $m/z = 331$ (Rhodamine), which indicates that most of the RhB is successfully transformed into CO₂ and H₂O in the photocatalytic process over TB-3.

3.3.2. Photocatalysis mechanism. Based on the mentioned experiments and characterization, a possible reaction mechanism is proposed in Fig. 9. The combination of 0D Bi₂O₂CO₃ QDs and 1D TiO₂ NBs reduces the band gap and improves the utilization of visible light. When TB-3 is irradiated by visible light, the excited e^- is transferred from the valence band (VB) to the conduction band (CB), leaving h^+ with high oxidative activity on the VB. Part of the h^+ directly reacts with RhB into CO₂ and H₂O. Some of the holes are captured by water molecules to generate $\cdot\text{OH}$, which is one of the main active species to degrade RhB. Furthermore, the introduced Bi₂O₂CO₃ endows the hybrid with faster electron transport rate and less recombination of charges. The QD architecture generated on the surface of 1D NBs acts as an electron acceptor and reservoir. The electrons can easily transfer from 1D TiO₂ NBs to Bi₂O₂CO₃ QDs, which facilitates the separation of the photo-generated carriers and further improves the photocatalytic activity.

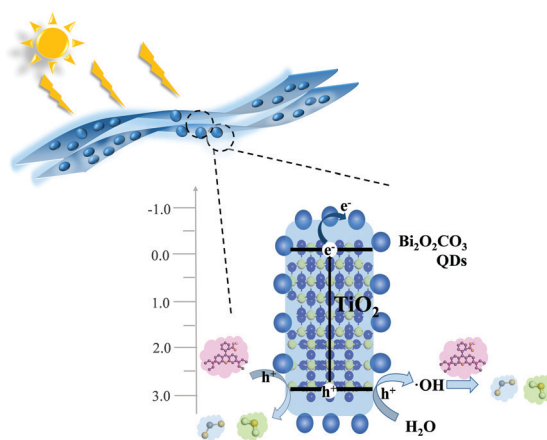


Fig. 9 Schematic illustration for the photocatalytic mechanism over the TB-3.

4. Conclusions

Herein, a novel Bi₂O₂CO₃/TiO₂ hybrid with 0D/1D nanostructure was successfully developed *via* a simple solvothermal method. It was verified by XRD and TEM that Bi₂O₂CO₃ QDs with a diameter of 1.4–1.5 nm uniformly grew on the surface of 1D TiO₂ NBs. The materials exhibit excellent photocatalytic performance on the degradation of RhB. Among them, TB-3 shows the best performance, achieving 95.34% degradation efficiency within 150 minutes. And the *K* is $18.51 \times 10^{-3} \text{ min}^{-1}$, which is nine times larger than that of the TiO₂ NBs. The preeminent performance may be attributed to the successful introduction of Bi₂O₂CO₃ QDs, which endows the material with more utilization of visible light, faster electronic transport rate and less recombination of carriers. In the photoreaction, h⁺ and •OH may be the main active species. And TB-3 shows superior stability and is not significantly deactivated in six cycles. Our work provides a new idea for the synthesis of the 0D/1D nanocomposite with excellent photocatalytic activity under visible light.

Author contributions

Yanwei Wang, Jiayi Li and Yang Li contributed to the conceptualization of the study. Yanwei Wang contributed to the formal analysis of the study. Bowei Wang, Yang Li and Guoyi Bai contributed to the funding acquisition of the study. Yang Li, Bowei Wang, Xilong Yan and Ligong Chen contributed to the project administration of the study. Yanwei Wang, Jiayi Li and Yang Li contributed to the writing – original draft of the study. Bowei Wang, Ligong Chen, Yang Li, Guoyi Bai and Mingming Sun contributed to the writing – review & editing of the study.

Conflicts of interest

There are no conflicts to declare.

Acknowledgements

Project funded by the National Natural Science Foundation of China (Grant No. 21808161 and 21978208), China Postdoctoral Science Foundation (Grant No. 2020T130465) and the Natural Science Foundation of Hebei Province (B2019201341).

Notes and references

- J. Fu, B. Zhu, C. Jiang, B. Cheng, W. You and J. Yu, *Small*, 2017, **13**.
- K. Singh and S. Arora, *Crit. Rev. Environ. Sci. Technol.*, 2011, **41**, 807–878.
- R. Khan, P. Bhawana and M. H. Fulekar, *Rev. Environ. Sci. Bio/Technol.*, 2013, **12**, 75–97.
- E. Forgacs, T. Cserhati and G. Oros, *Environ. Int.*, 2004, **30**, 953–971.
- H. Zangeneh, A. A. L. Zinatizadeh, M. Habibi, M. Akia and M. H. Isa, *J. Ind. Eng. Chem.*, 2015, **26**, 1–36.
- H. Cheng, B. Huang, K. Yang, Z. Wang, X. Qin, X. Zhang and Y. Dai, *ChemPhysChem*, 2010, **11**, 2167–2173.
- Z. Dong, L. Zhang, J. Gong and Q. Zhao, *Chem. Eng. J.*, 2021, 403.
- Q. Tang, R. Niu and J. Gong, *New J. Chem.*, 2020, **44**, 17405–17412.
- M. Sadeghi, S. Farhadi and A. Zabardasti, *New J. Chem.*, 2020, **44**, 20878–20894.
- A. Fujishima and K. Honda, *Nature*, 1972, **238**, 37–38.
- C. M. Teh and A. R. Mohamed, *J. Alloys Compd.*, 2011, **509**, 1648–1660.
- X. Liu, Z. Xing, Y. Zhang, Z. Li, X. Wu, S. Tan, X. Yu, Q. Zhu and W. Zhou, *Appl. Catal., B*, 2017, **201**, 119–127.
- U. Bach, D. Lupo, P. Comte, J. E. Moser, F. Weissortel, J. Salbeck, H. Spreitzer and M. Gratzel, *Nature*, 1998, **395**, 583–585.
- H. Y. Yang, S. F. Yu, S. P. Lau, X. Zhang, D. D. Sun and G. Jun, *Small*, 2009, **5**, 2260–2264.
- N. Wu, J. Wang, D. N. Tafen, H. Wang, J.-G. Zheng, J. P. Lewis, X. Liu, S. S. Leonard and A. Manivannan, *J. Am. Chem. Soc.*, 2010, **132**, 6679–6685.
- Z. Zhao, J. Tian, Y. Sang, A. Cabot and H. Liu, *Adv. Mater.*, 2015, **27**, 2557–2582.
- W. Zhou, G. Du, P. Hu, G. Li, D. Wang, H. Liu, J. Wang, R. I. Boughton, D. Liu and H. Jiang, *J. Mater. Chem.*, 2011, **21**, 7937–7945.
- J. Tian, Z. Zhao, A. Kumar, R. I. Boughton and H. Liu, *Chem. Soc. Rev.*, 2014, **43**, 6920–6937.
- X. Zhang, Y. Wang, B. Liu, Y. Sang and H. Liu, *Appl. Catal., B*, 2017, **202**, 620–641.
- Q. Tao, B. Wang, X. Yan and L. Chen, *Appl. Surf. Sci.*, 2019, **490**, 546–555.
- P. Madhusudan, J. Ran, J. Zhang, J. Yu and G. Liu, *Appl. Catal., B*, 2011, **110**, 286–295.
- Y. Ao, L. Xu, P. Wang, C. Wang, J. Hou, J. Qian and Y. Li, *Appl. Surf. Sci.*, 2015, **355**, 411–418.
- Q. Wang, G. Yun, Y. Bai, N. An, J. Lian, H. Huang and B. Su, *Appl. Surf. Sci.*, 2014, **313**, 537–544.
- Y. Lian, L. Ying, C. Li and H. Wang, *Dig. J. Nanomater. Bios.*, 2017, **12**, 1107–1117.
- Y. Xie, G. Ali, S. H. Yoo and S. O. Cho, *ACS Appl. Mater. Interfaces*, 2010, **2**, 2910–2914.
- H. Zhang, H. Ming, S. Lian, H. Huang, H. Li, L. Zhang, Y. Liu, Z. Kang and S.-T. Lee, *Dalton Trans.*, 2011, **40**, 10822–10825.
- Y.-F. Xu, M.-Z. Yang, B.-X. Chen, X.-D. Wang, H.-Y. Chen, D.-B. Kuang and C.-Y. Su, *J. Am. Chem. Soc.*, 2017, **139**, 5660–5663.
- H. Li, Y. Wang, G. Chen, Y. Sang, H. Jiang, J. He, X. Li and H. Liu, *Nanoscale*, 2016, **8**, 6101–6109.
- Y. K. Kho, A. Iwase, W. Y. Teoh, L. Maedler, A. Kudo and R. Amal, *J. Phys. Chem. C*, 2010, **114**, 2821–2829.
- D. C. Hurum, A. G. Agrios, K. A. Gray, T. Rajh and M. C. Thurnauer, *J. Phys. Chem. B*, 2003, **107**, 4545–4549.
- W. Fu, G. Li, Y. Wang, S. Zeng, Z. Yan, J. Wang, S. Xin, L. Zhang, S. Wu and Z. Zhang, *Chem. Commun.*, 2018, **54**, 58–61.

- 32 Z. W. Pan, Z. R. Dai and Z. L. Wang, *Science*, 2001, **291**, 1947–1949.
- 33 Y. Sun, Z. Zhao, F. Dong and W. Zhang, *Phys. Chem. Chem. Phys.*, 2015, **17**, 10383–10390.
- 34 J. Tian, Y. Leng, Z. Zhao, Y. Xia, Y. Sang, P. Hao, J. Zhan, M. Li and H. Liu, *Nano Energy*, 2015, **11**, 419–427.
- 35 F. Dong, S. C. Lee, Z. Wu, Y. Huang, M. Fu, W.-K. Ho, S. Zou and B. Wang, *J. Hazard. Mater.*, 2011, **195**, 346–354.
- 36 Z. Jiao, M. Shang, J. Liu, G. Lu, X. Wang and Y. Bi, *Nano Energy*, 2017, **31**, 96–104.
- 37 F.-X. Xiao, J. Miao and B. Liu, *J. Am. Chem. Soc.*, 2014, **136**, 1559–1569.
- 38 H. Yu, Y. Zhao, C. Zhou, L. Shang, Y. Peng, Y. Cao, L.-Z. Wu, C.-H. Tung and T. Zhang, *J. Mater. Chem. A*, 2014, **2**, 3344–3351.
- 39 G. Li, Z. Lian, W. Wang, D. Zhang and H. Li, *Nano Energy*, 2016, **19**, 446–454.
- 40 K. A. S. Fernando, S. Sahu, Y. Liu, W. K. Lewis, E. A. Gulians, A. Jafariyan, P. Wang, C. E. Bunker and Y.-P. Sun, *ACS Appl. Mater. Interfaces*, 2015, **7**, 8363–8376.
- 41 F. Amano, A. Yamakata, K. Nogami, M. Osawa and B. Ohtani, *J. Am. Chem. Soc.*, 2008, **130**, 17650–17651.
- 42 T. Watanabe, T. Takizawa and K. Honda, *J. Phys. Chem.*, 1977, **81**, 1845–1851.